Pressure-dependent electronic structures in multiferroic $DyMnO_3$: A combined lifetime-broadening-suppressed x-ray absorption spectroscopy and *ab initio* electronic structure study

J. M. Chen,[1,a),b)] J. M. Lee,[1,2] T. L. Chou,[1] S. A. Chen,[1] S. W. Huang,[1,2] H. T. Jeng,[3,a),c)] K. T. Lu,[1] T. H. Chen,[1] Y. C. Liang,[1] S. W. Chen,[1] W. T. Chuang,[1] H.-S. Sheu,[1] N. Hiraoka,[1] H. Ishii,[1] K. D. Tsuei,[1] Eugene Huang,[4] C. M. Lin,[5] and T. J. Yang[2]

[1]*National Synchrotron Radiation Research Center (NSRRC), Hsinchu 30076, Taiwan, Republic of China*
[2]*Department of Electrophysics, National Chiao Tung University, Hsinchu 30010, Taiwan, Republic of China*
[3]*Institute of Physics, Academia Sinica, Taipei 11529, Taiwan, Republic of China*
[4]*Center for General Education, Chung Chou Institute of Technology, Changhua County 510, Taiwan, Republic of China*
[5]*Department of Applied Science, National Hsinchu University of Education, Hsinchu 30014, Taiwan, Republic of China*

(Received 18 March 2010; accepted 26 August 2010; published online 19 October 2010)

Variations in the electronic structure and structural distortion in multiferroic $DyMnO_3$ were probed by synchrotron x-ray diffraction, lifetime-broadening-suppressed x-ray absorption spectroscopy (XAS), and *ab initio* electronic structure calculations. The refined x-ray diffraction data enabled an observation of a diminished local Jahn–Teller distortion of Mn sites within MnO_6 octahedra in $DyMnO_3$ on applying the hydrostatic pressure. The intensity of the white line in Mn *K*-edge x-ray absorption spectra of $DyMnO_3$ progressively increased with the increasing pressure. With the increasing hydrostatic pressure, the absorption threshold of an Mn *K*-edge spectra of $DyMnO_3$ shifted toward a greater energy, whereas the pre-edge line slightly shifted to a smaller energy. We provide the spectral evidence for the pressure-induced bandwidth broadening for manganites. The intensity enhancement of the white line in Mn *K*-edge spectra is attributed to a diminished Jahn–Teller distortion of MnO_6 octahedra in compressed $DyMnO_3$. A comparison of the pressure-dependent XAS spectra with the *ab initio* electronic structure calculations and full calculations of multiple scattering using the code FDMNES shows the satisfactory agreement between experimental and calculated Mn *K*-edge spectra. © *2010 American Institute of Physics*. [doi:10.1063/1.3490400]

I. INTRODUCTION

Perovskite manganites $RMnO_3$ and hole-doped manganites of composition $R_{1-x}A_xMnO_3$ (rare-earth ions R and alkaline-earth ions A) exhibit fascinating physical properties, such as charge and orbital ordering,[1–3] metal-insulator transitions,[4] colossal magnetoresistance,[5–9] half-metallic behavior,[10,11] percolative phase separation,[12–16] and multiferroicity.[17–24] In many such phenomena, the electronic properties are related intimately to the crystal lattice, through a complicated interplay between the crystal lattice, spin, charge, and orbital degrees of freedom.[25–29] In particular, magnetoelectrics, in which magnetism and ferroelectricity coexist and are mutually coupled have attracted renewed attention because of both their intrinsic scientific interest and prospective applications in novel magnetoelectric and magneto-optical devices. The magnetoelectric effect signifies an electric polarization generated with a magnetic field or a magnetization generated with an electric field in a material. Multiferroicity has been observed in such manganites as $TbMnO_3$, $DyMnO_3$, and $TbMn_2O_5$.[17–19]

Figure 1 shows the crystal structure of orthorhombic $DyMnO_3$. The perovskite $DyMnO_3$ structure contains the corner-sharing MnO_6 octahedra with the Mn ion at their centers and Dy occupying holes between the octahedra. The small radius of the Dy ion in $RMnO_3$ produces a cooperative buckling and tilting of the corner-shared MnO_6 octahedra known as $GdFeO_3$ distortions. At an ambient pressure and temperature, the perovskite $DyMnO_3$ structure distorts to orthorhombic *Pbnm* symmetry. The MnO_6 octahedron in $DyMnO_3$ is highly distorted, and tilted with an average Mn–O–Mn bond angle of ~145° in the plane to be compared with a value of ~155° in $LaMnO_3$. The Jahn–Teller (JT) distortion of the $Mn^{3+}O_6$ octahedra in $DyMnO_3$ produces Mn–O bonds in three pairs: one Mn–O1 for apical bonds along the *c* axis, and two Mn–O2 for equatorial bonds in the *ab* plane. In the basal *ab* plane, long Mn–O2(*l*) (2.22 Å) and short Mn–O2(*s*) bonds (1.89 Å) alternate.

$DyMnO_3$ shows an incommensurate crystallographic superstructure below the Néel temperature (T_N=39 K) corresponding to a sinusoidal antiferromagnetic ordering of the

[a)]Authors to whom correspondence should be addressed.
[b)]Electronic mail: jmchen@nsrrc.org.tw.
[c)]Electronic mail: jeng@phys.sinica.edu.tw

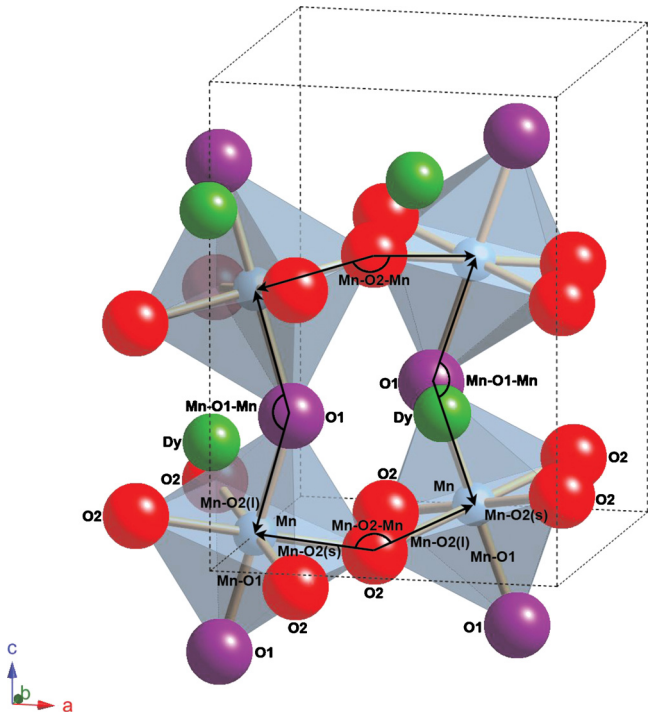

FIG. 1. Crystal structure of $DyMnO_3$.

Mn moments along the *b* axis. The transition ($T \sim 18$ K) to a noncollinear spiral magnetic ordering in which inversion symmetry is broken is accompanied with a large spontaneous electric polarization along the *c* axis ($\sim 2 \times 10^{-3}$ C m^{-2}).[30] The appearance of ferroelectricity at the transition into the spiral structure of $RMnO_3$ with R=Tb, Dy, and Gd was explained microscopically in terms of a spin supercurrent according to $P_e = \eta e_{ij} \times (S_i \times S_j)$, in which appear electric polarization P_e, magnetic moments S_i and S_j, the unit vector $\mathbf{e}_{ij}$ connecting sites *i* and *j*, and factor η, which is proportional to the transfer integral.[31] The magnetoelectric effect is thus correlated closely with the noncollinear spin configurations induced by a significant cooperative Jahn–Teller distortion of MnO_6 octahedra and a large octahedral tilt angle.[32] The JT distortion and tilt angle of MnO_6 octahedra in $DyMnO_3$ can become modified when smaller ions or divalent cations are incorporated into the rare-earth sites or when hydrostatic pressure is applied.[33] In addition to the induced structural disorders, doping with divalent cations or monovalent cations into rare-earth sites in $RMnO_3$ generally complicates the electronic structure, producing mixed valence states or oxygen-deficient states.[33,34] External pressure is therefore an ideal tool to tune the extent of the JT distortion in rare-earth manganites.

The insulator-metal transition (IMT) of rare-earth manganites mediated with an external hydrostatic pressure is reported.[35,36] The variation of electron bandwidth under hydrostatic pressure is proposed to serve as a driving force to induce the IMT of rare-earth manganites,[35] but the spectral evidence for a pressure-induced bandwidth variation of manganites is still sparse. X-ray absorption spectra (XAS) with chemical selectivity provide insight complementary to diffraction measurements into the local environment around an absorber atom of a material under pressure. The *K*-edge absorption spectra of transition-metal oxides reveal a strong dependence on the charge distribution and symmetry distortions of the probed site in a material,[37–39] but 1*s* core-hole lifetime broadening (>1.15 eV) in absorption precludes obtaining the spectra at high resolution, particularly the pre-edge features in the *K*-edge absorption spectra of transition-metal compounds.

In this work, we applied techniques derived from a resonant inelastic x-ray scattering called the lifetime broadening suppressed x-ray absorption spectroscopy in the partial fluorescence yield.[40] The *K*-edge XAS spectra at high resolution, particularly in the pre-edge region, provide an accurate spectral information about the electronic structure and local structure of a material under pressure. The dependence of the orthorhombic *Pbnm* perovskite structure of $RMnO_3$ (R=Dy, Gd, and Tb) on temperature and magnetic field is known,[17–19] but the effect of hydrostatic pressure on highly distorted multiferroic $DyMnO_3$ is less investigated. In this work, we probed the variations of electronic structure and structural distortion in orthorhombic $DyMnO_3$ under external hydrostatic pressure using combined XAS and x-ray diffraction (XRD) techniques. The pressure-dependent Mn *K*-edge XAS spectra were compared with the results of the *ab initio* electronic structure calculations and full multiple-scattering calculations using the code FDMNES.[41]

II. EXPERIMENTS

Polycrystalline $DyMnO_3$ was synthesized with a conventional citrate-gel process. Dy_2O_3 and MnO in stoichiometric proportions were dissolved in aqueous solutions of citric and nitric acids. The solution was heated at 95 °C until a spongy gel was formed, and then heated at a higher temperature to produce dark-colored ashes. These ground ashes were first calcinated at 600 °C in air to remove organic residues, and then further calcinated 950 °C in air for 12 h to obtain adequate crystallinity. Orthorhombic $DyMnO_3$ of satisfactory quality was used for the subsequent high pressure experiments.

The dependence of an Mn *K*-edge x-ray absorption on pressure was measured at the Taiwan inelastic x-ray scattering beamline BL12XU in SPring-8.[42] The synchrotron radiation from an undulator was made monochromatic with a Si(111) double-crystal monochromator and focused to a spot $\sim 16 \times 20$ μm^2 full width at half maximum (FWHM) in a diamond-anvil pressure cell using two mirrors in a Kilpatrick–Baez (KB) geometry. The emitted x-ray fluorescence was analyzed with a spectrometer comprising a synchronously moving, spherically bent Si (440) analyzer and a photon-counting detector on the 1-m-armed Rowland circle. The overall resolution, which is evaluated from the quasi-elastic scattering from the sample, had a FWHM of 0.9 eV. The incident energy was calibrated with the known Mn *K*-edge absorption inflection point at 6539 eV of an Mn foil. A sample $DyMnO_3$ as a finely grained powder was loaded into a hole (diameter 100 μm) of a Be gasket mounted on a Mao-Bell type diamond anvil cell (culet size 550 μm). Silicone oil served as a medium to transmit pressure. All measurements were performed at room temperature. The applied

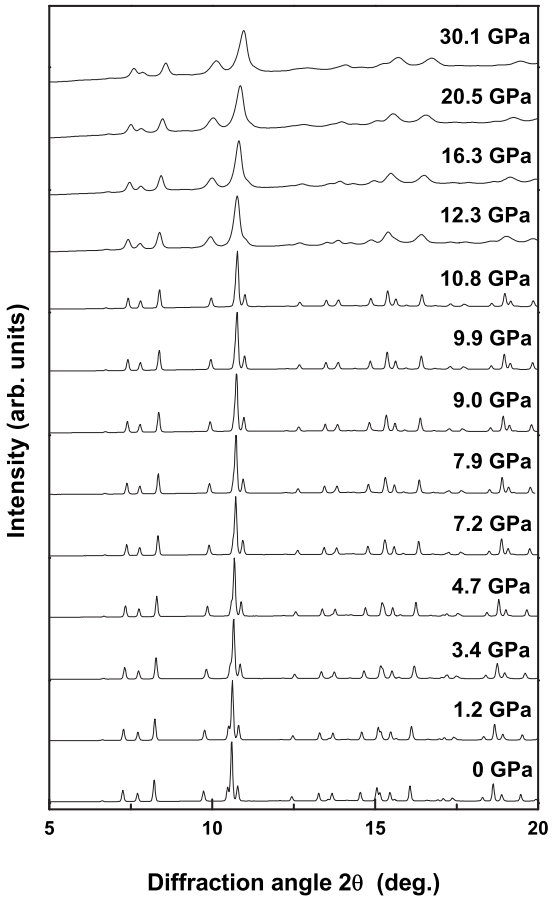

FIG. 2. Representative x-ray diffraction patterns of orthorhombic $DyMnO_3$ for hydrostatic pressure in a range ambient to ~30 GPa.

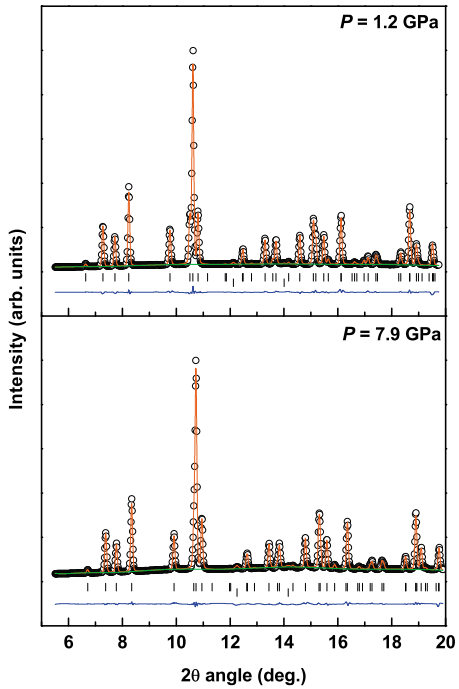

FIG. 3. X-ray diffraction patterns for $DyMnO_3$ (circles) with their Rietveld refinement (solid line) and residuals for pressures (a) $P=1.2$ GPa and (b) $P=7.9$ GPa. The first row of the vertical marks at an individual pressure corresponds to calculated peak positions of $DyMnO_3$ and the second row to the Au reference as a pressure indicator.

hydrostatic pressure was averaged at multiple points through the line shift of the ruby luminescence before and after each spectral collection.

The pressure-dependent x-ray diffraction was measured at the beamline BL01C2 of National Synchrotron Radiation Research Center (NSRRC) in Taiwan. The incident x rays (wavelength 0.4959 Å, 25 keV) were generated from the superconducting wavelength-shifter beamline with a Si(111) double-crystal monochromator. The $DyMnO_3$ powder as grown was filled into the pinhole (diameter of 235 μm) of a stainless-steel gasket with an Au powder as a pressure indicator and a mixture of methanol-ethanol-water (16:3:1) as a pressure-transmitting medium in a diamond anvil cell (Mao-Bell type, culet size 550 μm). An Au powder standard was used to determine precisely the wavelength and the distance from the sample to the detector. The XRD pattern was recorded with a MAR345 imaging plate (exposure duration typically of ~20 min). The one-dimensional XRD pattern was converted with program FIT2D. The x-ray diffraction data was structurally refined with the Rietveld method as implemented in the general structure analysis system software package.

III. RESULTS AND DISCUSSION

In Fig. 2, the representative x-ray diffraction patterns of orthorhombic $DyMnO_3$ over the hydrostatic pressure range ambient to ~30 GPa at room temperature were reproduced. Because of the decreased size of particles and the pressure gradients in the sample upon applying an external pressure, the x-ray diffraction peaks exhibit a gradual broadening with an increasing pressure, as shown in Fig. 2.[43] In the entire range of pressure up to 30 GPa, the crystal structure of $DyMnO_3$ retains its initial *Pbnm* symmetry.

To deduce the complete crystal structure including lattice parameters and atomic positions, we refined the x-ray powder diffraction data with the Rietveld method up to ~8 GPa. Figure 3 shows typical XRD patterns recorded at $P=1.2$ and 7.8 GPa with their corresponding Rietveld refinement. The experimental XRD data and their Rietveld refinement agreed satisfactorily according to the small magnitudes of the residuals. The structural parameters of $DyMnO_3$ calculated from the diffraction data for selected pressures are given in Table I. Experimental XRD data and their Rietveld refinement agreed satisfactorily according to the small values of reliability parameters R_{wp}, R_p, and χ^2 shown in Table I. The values of structural parameters obtained at ambient pressure agree satisfactorily with those in the literature.[44]

To illuminate the detailed pressure-induced structural distortion, we demonstrate in Fig. 4 the pressure dependence of Mn–O distances including the apical distance Mn–O1 and equatorial distances Mn–O2, and the in-plane Mn–O2–Mn bond angle. These values are deduced from the structural parameters in Table I. As noted from Fig. 4(a), the short equatorial bond Mn–O2(s) and the apical distance Mn–O1 remain virtually constant for a hydrostatic pressure less than 8 GPa, which is the largest effect being a shortening of the long equatorial bond Mn–O2(l).

This condition indicates that the Jahn–Teller distortion of

TABLE I. Room-temperature structural parameters for $DyMnO_3$ (*Pbnm*) at four selected pressures calculated from the x-ray diffraction data.

P (GPa)	0	1.2	4.7	7.9
		Lattice parameters		
a(Å)	5.279 65(9)	5.265 81(8)	5.227 91(12)	5.197 85(11)
b(Å)	5.844 20(10)	5.826 11(9)	5.775 75(14)	5.738 49(12)
c(Å)	7.377 31(12)	7.366 45(11)	7.336 34(17)	7.312 01(15)
Volume	227.629(7)	225.996(6)	221.522(9)	218.101(8)
		Atomic positions		
Dy(x)	0.982 42(30)	0.982 77(25)	0.980 70(40)	0.981 90(40)
Dy(y)	0.082 66(17)	0.082 32(14)	0.082 04(23)	0.080 86(19)
O1(x)	0.1169(16)	0.1209(14)	0.1198(25)	0.1165(20)
O1(y)	0.4637(17)	0.4672(14)	0.4661(25)	0.4640(21)
O2(x)	0.2061(11)	0.2074(12)	0.2018(21)	0.2070(18)
O2(y)	0.1743(10)	0.1767(12)	0.1791(21)	0.1824(17)
O2(z)	0.5530(9)	0.5544(7)	0.5525(14)	0.5550(11)
		Reliability factors		
R_p(%)	2.40	2.23	2.46	2.13
R_{wp}(%)	3.53	3.10	3.97	3.11
χ^2	0.76	0.55	1.19	0.78

the MnO_6 octahedra in $DyMnO_3$ becomes suppressed upon applying an external hydrostatic pressure. A similar observation is reported for $LaMnO_3$ under hydrostatic pressure.[45] As noted from Fig. 4(b), the Mn–O2–Mn bond angle increases monotonically with an increasing hydrostatic pressure. Accordingly, the in-plane Mn–O2–Mn tilt angle of two adjacent MnO_6 octahedra [i.e., (180°—Mn–O2–Mn bond angle)/2] decreases monotonically with an increasing pressure. From the observation in Fig. 4, we infer a gradual symmetrization of the MnO_6 JT-distorted octahedra in $DyMnO_3$ with an increasing pressure.

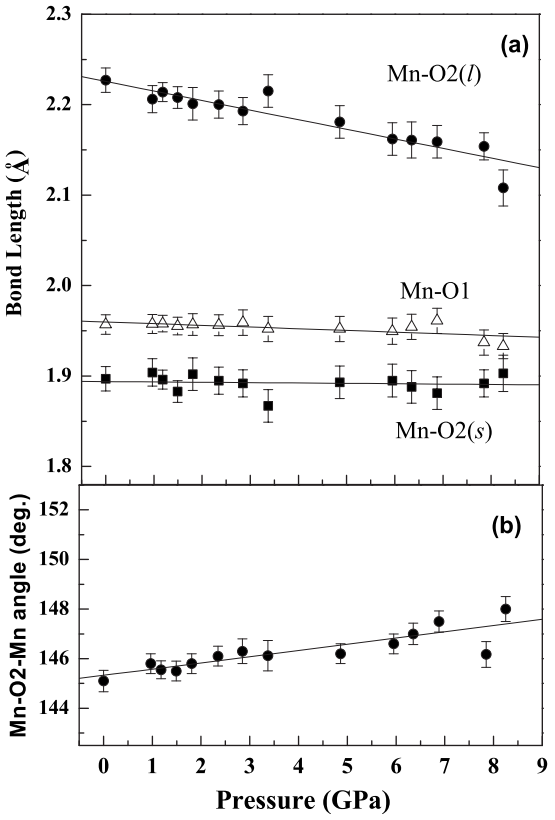

FIG. 4. Pressure dependence of (a) Mn–O distances including apical distance Mn–O1 and equatorial distance Mn–O2, and (b) Mn–O2–Mn bond angle of distorted MnO_6 octahedra in $DyMnO_3$.

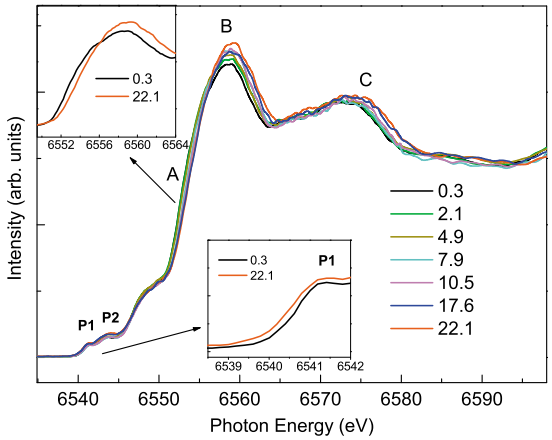

FIG. 5. High-resolution Mn *K*-edge XAS spectra, recorded by the partial fluorescence yield, of polycrystalline $DyMnO_3$ at various pressures up to ~22 GPa. The insets show an enlarged pre-edge region and near the threshold.

In Fig. 5, the high-resolution Mn *K*-edge XAS spectra of polycrystalline $DyMnO_3$ collected at various pressures up to ~22 GPa were reproduced. The spectra were obtained as a partial fluorescence yield with the spectrometer energy fixed at the maximum of the Mn $K\beta_{13}$ line. The Mn *K*-edge XAS spectrum of $DyMnO_3$ at ambient pressure contains two well resolved prepeaks in the pre-edge region (labeled P1 and P2) and an asymmetric white line (labeled B) with a shoulder on the side of small energy, and a broad peak (labeled C) at a greater photon energy.

As noted from Fig. 5, the Mn *K*-edge XAS spectra of $DyMnO_3$ at various pressures exhibit only a slight modification, implying that the local atomic environment about Mn in $DyMnO_3$ is not greatly altered under an external hydrostatic pressure up to ~22 GPa, which is consistent with the present XRD results. With an increasing external pressure, the intensity of the white line labeled B (6555–6565 eV) in the Mn *K*-edge spectra of $DyMnO_3$ increased progressively, whereas the shoulder of the white line became gradually suppressed, as shown in the insets of Fig. 5. At a greater pressure, the shape of the white line gradually became symmetric. With an increasing hydrostatic pressure, the absorption threshold labeled A and the broad peak labeled C in the Mn *K*-edge spectra of $DyMnO_3$ continuously shifted toward greater energy, whereas the pre-edge peak labeled P1 gradually shifted to smaller energy. Pre-edge peak P1 in Fig. 5 at $P=22$ GPa shifted to a smaller energy, ~0.3 eV, which is relative to that at $P=0.3$ GPa, as shown in the insets of Fig. 5.

To ensure an accurate assignment of the pre-edge features labeled P1 and P2 in Fig. 4, we performed band-structure calculations for orthorhombic $DyMnO_3$ in an A-type antiferromagnetic structure based on the experimental lattice parameters, as listed in Table I with 20 atoms in the

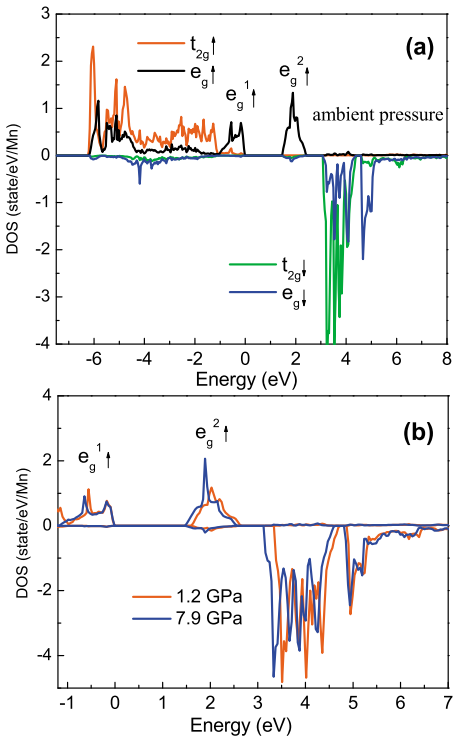

FIG. 6. (a) Partial densities of states of Mn projected onto fivefold 3*d* orbitals at ambient pressure and (b) partial density of states of Mn 3*d* states for $DyMnO_3$ at $P=1.2$ and 7.9 GPa for an hypothetical A-type antiferromagnetic structure of orthorhombic $DyMnO_3$ calculated with the GGA+U method. The parameters in these calculations are described in the text. For each panel the upper half denotes the majority and the lower half the minority spin states. The energy zero is at the Fermi energy (E_f).

unit cell. The band-structure calculations were performed using the full-potential projected augmented wave method implemented in the Vienna *ab initio* simulation package within the generalized gradient approximation plus on-site Coulomb interaction U (GGA+U) scheme.[46,47] In the GGA+U calculations, the Coulomb energy U=5.0 eV and exchange parameter J=0.87 eV for Mn 3*d* electrons were used.[48] A $(7\times7\times5)$ Monkhorst–Pack grid in the first Brillouin-zone which corresponds to 79 k-points in the irreducible part of the Brillouin-zone and the cutoff energy of 400 eV for the plane waves are chosen for present calculations. The convergence of the k-point sampling and cutoff energy is confirmed by comparing the results with those from a $(8\times8\times6)$ k-point mesh (92 k-points) with cutoff energy of 500 eV.

In the perovskite manganites $DyMnO_3$, the Mn^{3+} ion has a d^4 configuration. In an octahedral symmetry, the Mn 3*d* levels split into three lower-lying t_{2g} (d_{xy}, d_{yz}, and d_{zx}) and two higher-lying e_g orbitals. The Mn^{3+} ion has a high-spin configuration, with three electrons occupying the three t_{2g} orbitals and one electron occupying the doubly degenerate e_g orbitals as $t_{2g}{}^3e_g{}^1$. The degeneracy of the e_g orbital in $DyMnO_3$ perovskites is removed by a cooperative Jahn–Teller distortion. The e_g doublet is split further into two subbands $e_g{}^1\uparrow$ and $e_g{}^2\uparrow$ resulting from a strong Jahn–Teller distortion.

Figure 6(a) displays the partial density of states of fivefold Mn 3*d* states for $DyMnO_3$. There is an indirect gap between the JT-split Mn $e_g{}^1\uparrow$ and $e_g{}^2\uparrow$ bands. Based on the GGA+U calculations, the occupied $e_g{}^1\uparrow$ and unoccupied $e_g{}^2\uparrow$ bands (~2 eV above E_f) are dominated by $d_{3x^2-r^2}$ and $d_{y^2-z^2}$ orbitals, respectively, in one coplanar Mn ion, whereas they exhibit predominantly $d_{3y^2-r^2}$ and $d_{x^2-z^2}$ character, respectively, for the other coplanar Mn ion. A strong orbital polarization in the e_g band for $DyMnO_3$ with a staggered $d_{3x^2-r^2}/d_{3y^2-r^2}$-type orbital ordering pattern in the *ab* plane is clearly revealed.

For the spin-down channel, one $e_g\downarrow$ band ($d_{3z^2-r^2}$) is mixed with the $t_{2g}\downarrow$ bands at 3–4 eV above E_f, whereas the other $e_g\downarrow$ band ($d_{x^2-y^2}$) is located ~4.5 eV above E_f. The half-filled $e_g{}^1\uparrow$ orbitals of Mn^{3+} ions are located at the long Mn–O2(*l*) site projected predominantly along the *b* axis, whereas unoccupied $e_g{}^2\uparrow$ orbitals occupy the short Mn–O2(*s*) site projected predominantly along the *a* axis. The splitting of the $e_g\uparrow$ orbitals in the $t_{2g}{}^3e_g{}^1$ electron configuration of the Mn^{3+} ions is therefore closely related to the JT distortion and the orbital ordering within the MnO_6 octahedra in $DyMnO_3$. Figure 6(b) displays the partial density of states of fivefold Mn 3*d* states for $DyMnO_3$ at $P=1.2$ and 7.9 GPa. The structural parameters of $DyMnO_3$ at pressures 1.2 and 7.9 GPa are listed in Table I. The electronic band of the $e_g\uparrow$ orbitals and $t_{2g}\downarrow$ in $DyMnO_3$ under pressure is slightly broadened and shifted to lower energy.

The $1s\rightarrow3d$ transitions are generally considered to be weakly allowed either through a quadrupole interaction or via hybridization of the Mn 3*d* states with 4*p* states.[49] Based on the band structure calculations, P1 in Fig. 5 is ascribed to transitions of Mn 1*s* core electrons into unoccupied, majority-spin Mn $e_g\uparrow$ states hybridized with neighboring Mn 4*p* states. P2 in Fig. 5 is assigned as a superposition of transitions into empty, minority-spin $t_{2g}\downarrow$ and $e_g\downarrow$ states hybridized with neighboring 4*p* states. The white line, labeled B in Fig. 5, is attributed to transitions from Mn 1*s* to Mn 4*p* states. Feature C in Fig. 5 gains intensity from the multiple-scattering contribution of MnO_6 surrounded by eight Dy.

As shown in Fig. 4, the pressure effect is most pronounced for the long equatorial distance Mn–O2(*l*) that relates to the larger compressibility along the *b* axis under pressure. The compressive anisotropy of MnO_6 octahedra in $DyMnO_3$ upon applying hydrostatic pressure leads to a modified density of states. The electronic bandwidth of $e_g\uparrow$ orbitals is a key parameter to drive the insulator-metal transition of manganites.[35,45] The bandwidth of the $e_g\uparrow$ orbitals in manganites is closely related to the overlap between the Mn 3*d* and O 2*p* orbitals, and is highly correlated with the local atomic structure of MnO_6 octahedra including the equatorial bond distance Mn–O2 and the in-plane Mn–O2–Mn tilt angle.[50] The equatorial Mn–O2 distance and Mn–O2–Mn tilt angle decreased under an external pressure, as confirmed by the present XRD measurements, enhance the hybridization of the Mn 3*d* and O 2*p* orbitals and are expected to broaden the electronic band of $e_g\uparrow$ orbitals in $DyMnO_3$.[47] The pre-edge line P1 originating from transitions of Mn 1*s* core electrons to unoccupied Mn $3d(e_g\uparrow)$ states is accordingly gradually shifted toward smaller energy when a hydrostatic pressure is applied, consistent with the present GGA+U calculations shown in Fig. 6(b).

Polarization-dependent Mn *K*-edge x-ray absorption spectra of $RMnO_3$ (R=Tb, Dy) single crystals were previously observed to exhibit a notable anisotropy along three crystallographic directions, $E\|a$, $E\|b$, and $E\|c$, particularly for the white-line region.[49] The white line in the polarized Mn *K*-edge spectrum of $DyMnO_3$ for the $E\|b$ polarization lies at an energy ~2.4 eV smaller than for polarizations $E\|a$ and $E\|c$, corresponding to a highly anisotropic Mn–O2 bonding within the *ab* plane and weak covalency along the *b* axis in $RMnO_3$ (R=Tb, Dy).[49] The origin of this energy difference is attributed to a Jahn–Teller distortion and orbital ordering of MnO_6 octahedra in $RMnO_3$ (R=Tb, Dy).[51] A significant energy separation for the maximum of the white line of the polarized Mn *K*-edge spectrum along $E\|b$ relative to $E\|a$ and $E\|c$ produces an asymmetric profile of the white line, with a shoulder on the side of small energy of the Mn *K*-edge spectrum for polycrystalline $DyMnO_3$ at ambient pressure.

When the long equatorial bond Mn−O2(*l*) projected predominantly along the *b* axis is greatly shortened with an increasing hydrostatic pressure and approaches the length of the short equatorial bond Mn−O2(*s*) projected predominantly along the *a* axis, as evident in Fig. 4(a), the absorption edge of the Mn *K*-edge spectrum for E$\|b$ of $DyMnO_3$ gradually shifts to greater energy. The separation for the maximum of the white line of the Mn *K*-edge spectra between $E\|b$ and $E\|a$ of $DyMnO_3$ decreases because of a diminished JT distortion of $DyMnO_3$ upon applying an external hydrostatic pressure. An increased overlap between the $E\|b$ spectrum and the $E\|a$ spectrum under hydrostatic pressure consequently generates an increased intensity of the white line in the Mn *K*-edge spectra of $DyMnO_3$,[52] as supported by the gradually suppressed shoulder of white line with pressure in Fig. 5.

With the FDMNES code, we performed the Mn *K*-edge XAS calculations on $DyMnO_3$ based on the structural parameters at various pressures in Table I. In the present XAS simulation, a muffin-tin (MT) full-multiple-scattering (FMS) approach was applied with a cluster radius $R=5$ Å. We found that a spherical cluster of radius 5 Å satisfactorily reproduces all features of the absorption spectrum. The FMS calculations were performed using the MT potential constructed from 10% overlapped MT spheres of the specified radii. Figure 7 shows simulated Mn *K*-edge XAS spectra of $DyMnO_3$ with varied hydrostatic pressures. The intensity of the white line clearly increases with an increasing pressure. As shown in the insets of Fig. 7 with an increasing hydrostatic pressure, the absorption threshold of simulated Mn *K*-edge spectra of $DyMnO_3$ shifts toward greater energy, whereas the pre-edge peak shifts to smaller energy. The experimental and calculated Mn *K*-edge spectra agree satisfactorily.

IV. CONCLUSION

Pressure-induced variations of electronic structure and Jahn–Teller distortion in highly distorted multiferroic $DyMnO_3$ were probed on combining x-ray powder diffraction and lifetime-broadening-suppressed x-ray absorption spectroscopy recorded in the partial fluorescence yield. With an increasing external pressure, the short equatorial bond distance Mn−O2(*s*) and the Mn–O1 apical distance remained virtually constant for a pressure less than 8 GPa, the largest effect being a shortening of the long equatorial bond Mn−O2(*l*). The in-plane Mn–O2–Mn tilt angle of two adjacent MnO_6 octahedra decreased monotonically upon applying hydrostatic pressure. Based on these XRD results, a local JT distortion of Mn sites within MnO_6 octahedra in $DyMnO_3$ becomes suppressed with an increasing hydrostatic pressure. The intensity of the white line in Mn *K*-edge x-ray absorption spectra of $DyMnO_3$ increased progressively with an increasing pressure, whereas the shoulder of the white line was gradually suppressed. With an increasing hydrostatic pressure, the absorption threshold of Mn *K*-edge spectra of $DyMnO_3$ shifted toward greater energy, whereas the pre-edge line shifted slightly to smaller energy. The intensity enhancement of the white line of Mn *K*-edge spectra is attributed to a diminished Jahn–Teller distortion of MnO_6 octahedra in $DyMnO_3$ when a hydrostatic pressure is applied. We provide spectral evidence for the pressure-induced band broadening for manganites. The comparison of XAS data with *ab initio* electronic structure calculations and full multiple-scattering calculations using code FDMNES shows satisfactory agreement between experimental and calculated Mn *K*-edge spectra.

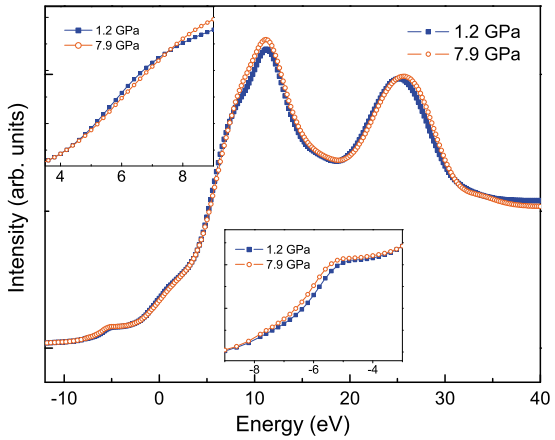

FIG. 7. Mn *K*-edge XAS spectra of $DyMnO_3$ with varied hydrostatic pressures simulated using code FDMNES for cluster radius $R=5$ Å. The insets show an enlarged pre-edge region and near the threshold.

ACKNOWLEDGMENTS

We thank the NSRRC staff for their technical support. This research is supported by the NSRRC and the National Science Council of the Republic of China under Grant Nos. NSC 96-2113-M-213-007 and NSC 98-2112-M-001-021.

[1] Y. Tokura and N. Nagaosa, Science **288**, 462 (2000).
[2] W. Luo, A. Franceschetti, M. Varela, J. Tao, S. J. Pennycook, and S. T. Pantelides, Phys. Rev. Lett. **99**, 036402 (2007).
[3] A. Tebano, C. Aruta, S. Sanna, P. G. Medaglia, G. Balestrino, A. A. Sidorenko, R. De Renzi, G. Ghiringhelli, L. Braicovich, V. Bisogni, and N. B. Brookes, Phys. Rev. Lett. **100**, 137401 (2008).
[4] M. Imada, A. Fujimori, and Y. Tokura, Rev. Mod. Phys. **70**, 1039 (1998).
[5] E. Dagotto, T. Hotta, and A. Moreo, Phys. Rep. **344**, 1 (2001).
[6] *Colossal Magnetoresistance Oxides*, edited by Y. Tokura (Gordon and

Breach, New York, 2000).
[7] R. von Helmolt, J. Wecker, B. Holzapfel, L. Schultz, and K. Samwer, Phys. Rev. Lett. **71**, 2331 (1993).
[8] S. Jin, T. H. Tiefel, M. McCormack, R. A. Fastnacht, R. Ramesh, and L. H. Chen, Science **264**, 413 (1994).
[9] Y. Tokura, A. Urushibara, Y. Moritomo, T. Arima, A. Asamitsu, G. Kido, and N. Furukawa, J. Phys. Soc. Jpn. **63**, 3931 (1994).
[10] W. E. Pickett and D. J. Singh, Phys. Rev. B **53**, 1146 (1996).
[11] M. S. Laad, L. Craco, and E. Müller-Hartmann, New J. Phys. **6**, 157 (2004).
[12] M. Fäth, S. Freisen, A. A. Menovsky, Y. Tomioka, J. Aart, and J. A. Mydosh, Science **285**, 1540 (1999).
[13] P. Levy, F. Parisi, L. Granja, E. Indelicato, and G. Polla, Phys. Rev. Lett. **89**, 137001 (2002).
[14] Ch. Simon, S. Mercone, N. Guiblin, C. Martin, A. Brûlet, and G. Andrè, Phys. Rev. Lett. **89**, 207202 (2002).
[15] M. Mayr, A. Moreo, J. A. Vergés, J. Arispe, A. Feiguin, and E. Dag, Phys. Rev. Lett. **86**, 135 (2001).
[16] M. B. Salamon and M. Jaime, Rev. Mod. Phys. **73**, 583 (2001).
[17] T. Kimura, T. Goto, H. Shintani, K. Ishizaka, T. Arima, and Y. Tokura, Nature (London) **426**, 55 (2003).
[18] N. Hur, S. Park, P. A. Sharma, J. S. Ahn, S. Guha, and S.-W. Cheong, Nature (London) **429**, 392 (2004).
[19] T. Goto, T. Kimura, G. Lawes, A. P. Ramirez, and Y. Tokura, Phys. Rev. Lett. **92**, 257201 (2004).
[20] N. A. Spaldin and M. Fiebig, Science **309**, 391 (2005).
[21] W. Eerenstein, N. D. Mathur, and J. F. Scott, Nature (London) **442**, 759 (2006).
[22] R. Ramesh and N. A. Spaldin, Nature Mater. **6**, 21 (2007).
[23] L. C. Chapon, G. R. Blake, M. J. Gutmann, S. Park, N. Hur, P. G. Radaelli, and S.-W. Cheong, Phys. Rev. Lett. **93**, 177402 (2004).
[24] M. Fiebig, J. Phys. D **38**, R123 (2005).
[25] A. J. Millis, Nature (London) **392**, 147 (1998).
[26] C. N. R. Rao, J. Phys. Chem. B **104**, 5877 (2000).
[27] S. W. Cheong and M. Mostovoy, Nature Mater. **6**, 13 (2007).
[28] P. M. Woodward, E. Suard, and P. Karen, J. Am. Chem. Soc. **125**, 8889 (2003).
[29] K. Kuepper, M. C. Falub, K. C. Prince, V. R. Galakhov, I. O. Troyanchuk, S. G. Chiuzbăian, M. Matteucci, D. Wett, R. Szargan, N. A. Ovechkina, Y. M. Mukovskii, and M. Neumann, J. Phys. Chem. B **109**, 9354 (2005).
[30] T. Kimura, G. Lawes, T. Goto, Y. Tokura, and A. P. Ramirez, Phys. Rev. B **71**, 224425 (2005).
[31] H. Katsura, N. Nagaosa, and A. V. Balatsky, Phys. Rev. Lett. **95**, 057205 (2005).
[32] T. Kimura, S. Ishihara, H. Shintani, T. Arima, K. T. Takahashi, K. Ishizaka, and Y. Tokura, Phys. Rev. B **68**, 060403 (2003).
[33] J. Blasco, C. Ritter, J. García, J. M. de Teresa, J. Pérez-Cacho, and M. R. Ibarra, Phys. Rev. B **62**, 5609 (2000).
[34] C. C. Yang, M. K. Chung, W.-H. Li, T. S. Chan, R. S. Liu, Y. H. Lien, C. Y. Huang, Y. Y. Chan, Y. D. Yao, and J. W. Lynn, Phys. Rev. B **74**, 094409 (2006).
[35] A. Yamasaki, M. Feldbacher, Y.-F. Yang, O. K. Andersen, and K. Held, Phys. Rev. Lett. **96**, 166401 (2006).
[36] V. Laukhin, J. Fontcuberta, J. L. Garcia-Munoz, and X. Obradors, Phys. Rev. B **56**, R10009 (1997).
[37] F. Bridges, C. H. Booth, M. Anderson, G. H. Kwei, J. J. Neumeier, J. Snyder, J. Mitchell, J. S. Gardner, and E. Brosha, Phys. Rev. B **63**, 214405 (2001).
[38] A. Yu. Ignatov, N. Ali, and S. Khalid, Phys. Rev. B **64**, 014413 (2001).
[39] T. Shibata, B. A. Bunker, and J. F. Mitchell, Phys. Rev. B **68**, 024103 (2003).
[40] J.-P. Rueff, L. Journel, P.-E. Petit, and F. Farges, Phys. Rev. B **69**, 235107 (2004).
[41] Y. Joly, Phys. Rev. B **63**, 125120 (2001).
[42] Y. Q. Cai, P. Chow, C. C. Chen, H. Ishii, K. L. Tsang, C. C. Kao, K. S. Liang, and C. T. Chen, AIP Conf. Proc. **705**, 340 (2004).
[43] Z. Wang, Y. Zhao, D. Schiferl, C. S. Zha, and R. T. Downs, Appl. Phys. Lett. **85**, 124 (2004).
[44] J. A. Alonso, M. J. Martínez-Lope, M. T. Casais, and M. T. Fernández-Díaz, Inorg. Chem. **39**, 917 (2000).
[45] I. Loa, P. Adler, A. Grzechnik, K. Syassen, U. Schwarz, M. Hanfland, G. Kh. Rozenberg, P. Gorodetsky, and M. P. Pasternak, Phys. Rev. Lett. **87**, 125501 (2001).
[46] G. Kresse and D. Joubert, Phys. Rev. B **59**, 1758 (1999).
[47] A. I. Liechtenstein, V. I. Anisimov, and J. Zaanen, Phys. Rev. B **52**, R5467 (1995).
[48] G. Giovannetti and J. van den Brink, Phys. Rev. Lett. **100**, 227603 (2008).
[49] J. M. Chen, C. K. Chen, T. L. Chou, I. Jarrige, H. Ishii, K. T. Lu, Y. Q. Cai, K. S. Ling, J. M. Lee, S. W. Huang, T. J. Yang, C. C. Shen, R. S. Liu, J. Y. Lin, H. T. Jeng, and C. C. Kao, Appl. Phys. Lett. **91**, 054108 (2007).
[50] C. Cui and T. A. Tyson, Appl. Phys. Lett. **84**, 942 (2004).
[51] I. S. Elfimov, V. I. Anisimov, and G. A. Sawatzky, Phys. Rev. Lett. **82**, 4264 (1999).
[52] A. Y. Ramos, H. C. N. Tolentino, N. M. Souza-Neto, J.-P. Itié, L. Morales, and A. Caneiro, Phys. Rev. B **75**, 052103 (2007).